COMPUTATIONAL HEAT FLUX PREDICTIONS FOR THE AFOSR BOLT-II FLIGHT TEST

A Thesis

by

ERIC LAWRENCE SWINNY

Submitted to the Graduate and Professional School of
Texas A&M University
in partial fulfillment of the requirements for the degree of

MASTER OF SCIENCE

Chair of Committee,	Rodney D.W. Bowersox
Committee Members,	Edward B. White
	Waruna D. Kulatilaka
Head of Department,	Srinivas R. Vadali

August 2021

Major Subject: Aerospace Engineering

ABSTRACT

The BOundary Layer Turbulence (BOLT-II) flight experiment proposed by the Air Force Office of Scientific Research (AFOSR) is a joint collaboration between academia, industry, and government partners to advance the understanding of hypersonic boundary layer turbulence on a concave surface with highly swept leading edges. To perform such a test at hypersonic speeds a large amount of aerodynamic analysis must be done before flight to assess the mechanical and thermal loads expected on the vehicle and analyze what effects they could have on the vehicle being flown. One of the largest challenges when performing these analyses is quantifying thermal loading on the transition between BOLT-II and the rocket system being flown on. To analyze these thermal loads a set of computational fluid dynamics (CFD) simulations were performed in the US3D code using structured grids generated in the Pointwise meshing software. A convergence study was performed on a quarter-symmetry mesh to iteratively design a mesh with the ability to simultaneously capture the laminar sub-layer and generate grid independent solutions of wall heat flux. The research in this thesis focuses on using these CFD simulations to quantify heat flux on the fairing and payload bay at critical points identified on the BOLT-II flight test trajectory in support of thermal protection (TPS) calculations at the Calspan-University of Buffalo Research Center (CUBRC) and Johns Hopkins University Applied Physics Laboratory (JHAPL). To determine the dependence of heat flux results on the selected turbulence models additional CFD simulations were run using an alternate turbulence model to quantify the difference in heat flux calculated using the two turbulence models. To analyze the validity of heat flux data CFD results were compared to heat flux calculated from wind tunnel tests on a 25 percent scale model of BOLT-II, the fairing, and sections of the payload bay using IR thermography and a 1D heat flux analysis code. This comparison showed agreement between major heat flux features observed in CFD and wind tunnel tests providing evidence that qualitatively supports CFD results. From these results recommendations are made concerning further tests that could be performed to improve information gained from this study.

ACKNOWLEDGMENTS

There are countless people that have supported and helped me during my time as a student at Texas A&M University. While the full list would be too big to include I would like to acknowledge some people that have been especially important to me during my studies.

To begin I would like to thank my adviser Dr. Bowersox for taking me on as a graduate student and helping to provide so many excellent learning experiences to me throughout my time in graduate school. I have been extremely grateful for his commitment to helping his students learn and succeed as both researchers and professionals. He always takes the time to help his students when they need it and never fails to bring a positive attitude to the table. I would also like to thank Dr. White and Dr. Kulatilaka for serving on my thesis committee.

I also have to thank the students at the NAL for always being supportive, helping me along the way, and making my time at the lab memorable. No matter what problems I ran into or what questions I had there was always someone at the lab willing to help or point me in the right direction. Special thanks especially goes to Heather Kostak and Bryan Morrealle who have been amazing research partners to work with on the BOLT-II flight test project; I will always be thankful for the endless help and support y'all have given me over the past two years. I would also like to thank Cecil Rhodes, Rebecca Marianno, and Colleen Leatherman for their hard work and organizational skills which keep the NAL running smoothly.

Finally I would like to thank my parents and my brother for their constant support throughout my education. I'm grateful for all the help and advice they have given, and continue to give, me to help me pursue my goals.

CONTRIBUTORS AND FUNDING SOURCES

Contributors

This work was supported by a thesis committee consisting of Dr. Rodney Bowersox (adviser) and Dr. Edward White of the Department of Aerospace Engineering and Dr. Waruna Kulatilaka of the Department of Mechanical Engineering.

Data for wind tunnel tests shown in this work was provided by Heather Kostak at Texas A&M University. Assistance in mesh generation using Pointwise for this analysis was provided by Bryan Morreale at Texas A&M University. Unless otherwise noted the analyses for this thesis were completed by the student independently.

Simulations performed in this thesis were conducted using the advanced computing resources provided by Texas A&M High Performance Research Computing.

Funding Sources

The work presented in this thesis was made possible by help from the United States Air Force Office of Scientific Research through grant FA9550-19-1-0154.

NOMENCLATURE

CFD	Computational Fluid Dynamics
BOLT-II	BOundary Layer Turbulence flight experiment
TPS	Thermal Protection System
AFOSR	Air Force Office of Scientific Research
CUBRC	Calspan University of Buffalo Research Center
JHAPL	Johns Hopkins University Applied Physics Laboratory
US3D	Unstructured 3D CFD code
CFL	Courant number
M_∞	Free stream Mach number
U_∞	Free stream velocity magnitude
$\vec{V}$	Velocity vector
u	X-component of velocity
v	Y-component of velocity
w	Z-component of velocity
α	Z-axis angle of attack
β	Y-axis angle of attack
Re	Reynolds number
St	Stanton number
L	Characteristic length
q_w	Wall heat flux
ρ	Density
ρ_∞	Free stream density

T	Temperature
T_∞	Free stream temperature
T_w	Wall temperature
T_{aw}	Adiabatic wall temperature
p	pressure
p_∞	Free stream pressure
R	Ideal gas constant for air
μ	Dynamic viscosity
μ_0	Reference dynamic viscosity
S	Sutherland temperature
γ	Ratio of specific heats
$Y+$	Dimensionless wall distance ("*y plus*")
h	Specific enthalpy
k	Thermal conductivity
c_p	Specific heat at constant pressure
ξ	Thermal diffusivity
δ	Boundary layer height

TABLE OF CONTENTS

Page

LIST OF FIGURES

FIGURE Page

LIST OF TABLES

TABLE Page

1. INTRODUCTION

1.1 Motivation

When designing and analyzing hypersonic vehicles understanding the effects of the boundary layer is critical due to its influence on aerodynamic heating, the mechanical loads experienced in flight, shock-boundary layer interaction, and turbulence around the vehicle. The mechanisms of turbulence in hypersonic flow are still not fully understood making rigorous analysis of these parameters expensive and difficult in many cases [1]. Most modern analysis methods for hypersonics rely on a combination of computational models and wind tunnel tests however each of these methods can still introduce degrees of uncertainty compared to actual flight conditions. The BOundary Layer Turbulence (BOLT-II) flight experiment is an attempt to reduce some of these uncertainties and further advance the understanding of turbulence at hypersonic speeds.

1.2 Background

The BOLT-II flight test is a unique collaboration between academia, industry, and government to improve the understanding of, and ability to model, hypersonic boundary layer turbulence on a concave surface with highly swept leading edges. The data produced by the BOLT-II flight test, and subsequent analyses of that data, will serve as a scientific heat flux benchmark for hypersonic turbulence which can be used to improve future works in hypersonics. Views of the BOLT-II geometry are shown in Figure 1.1 and the flight test vehicle is shown in Figure 1.2.

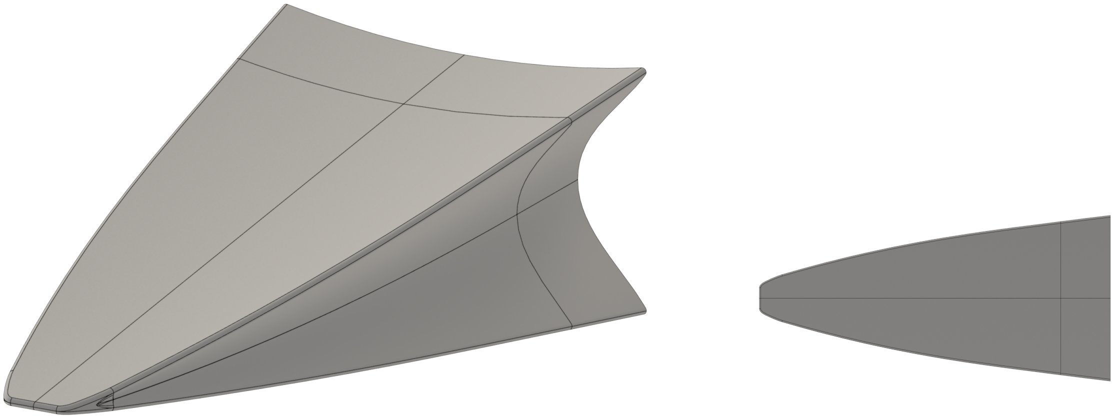

Figure 1.1: The BOLT-II experimental geometry

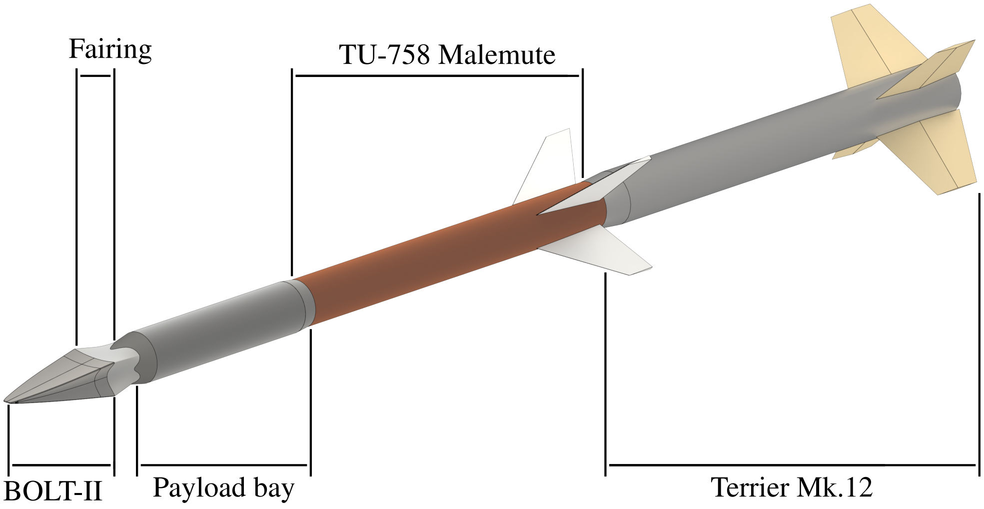

Figure 1.2: The BOLT-II flight test vehicle

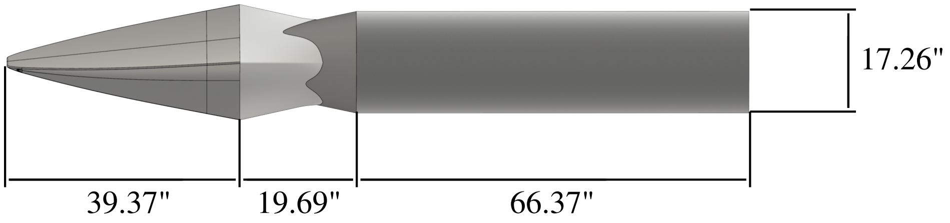

Figure 1.3: Geometry simulated in the BOLT-II heating study dimensioned in inches

The BOLT-II flight geometry was developed as a continuation of the BOLT geometry and is second derivative continuous across the surface of the vehicle to allow the flow to naturally form a turbulent boundary layer. The BOLT geometry was designed to present many unique challenges in aerodynamic modeling with its concave surfaces and highly swept leading edges [2]. The unique shape of the BOLT-II geometry specifically induces crossflow instabilities making it difficult to predict turbulent flow features using current methods [3].

The most basic explanation of why boundary layer heat flux is a significant factor at hypersonic speeds is due to to the amount of kinetic energy contained by the free stream. To enforce the no-slip condition on the wall of the vehicle the velocity must be reduced to zero in the boundary layer leading to the large amount of kinetic energy transforming to different forms, such as enthalpy, to satisfy the first law of thermodynamics [4][5]. One of the ways this energy transfer is manifested is by increasing the temperature of the fluid which often makes the temperature of the fluid near the wall much higher than that of the wall itself leading to net heat transfer into the wall [6]. While the concepts driving boundary layer heat transfer are easily explained on a basic level modeling and analyzing the behavior of boundary layers and heat flux is often not as simple.

In its simplest and earliest form the analysis of a boundary layer was performed for a steady state incompressible 2D flow over a flat plate with a laminar boundary layer [7]. For these flows it is assumed that the effects of viscosity are confined to a thin boundary layer near the surface of the wall [6]. The general setup of this system is illustrated in Figure 1.4.

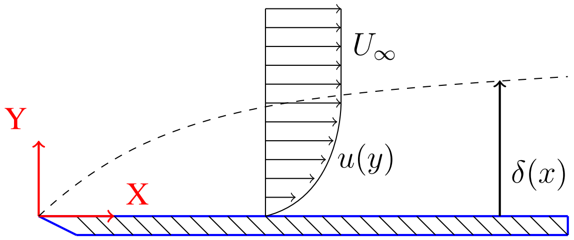

Figure 1.4: Boundary layer of a flat plate

From the assumptions for this system and the no-slip and no-penetration boundary conditions at the wall the full set of Navier Stokes equations can be simplified to the boundary layer equations. This set of equations was proposed by Ludwig Prandtl in 1904 and is the basis of many of the theories used when studying boundary layers [7][8]. The reduced equations are shown below where Equation 1.1 is continuity, Equation 1.2 is X-momentum, Equation 1.3 is Y-momentum, and Equation 1.4 stems from the energy equation.

$$\frac{\partial u}{\partial x} + \frac{\partial v}{\partial y} = 0 \tag{1.1}$$

$$\rho u \frac{\partial u}{\partial x} + \rho v \frac{\partial u}{\partial y} = -\frac{\partial p}{\partial x} + \mu \frac{\partial^2 u}{\partial y^2} \tag{1.2}$$

$$\frac{\partial p}{\partial y} = 0 \tag{1.3}$$

$$\rho u \frac{\partial h}{\partial x} + \rho v \frac{\partial h}{\partial y} = k \frac{\partial^2 T}{\partial y^2} + u \frac{\partial p}{\partial x} + \mu \left(\frac{\partial u}{\partial y} \right)^2 \tag{1.4}$$

An iterative method to solve for boundary layer characteristics from these equations was proposed a few years later by Blasius in 1908 using self-similar solutions [9]. Over the years a large number of different iterative methods used to solve the boundary layer equations has been proposed which have been tailored to have varying degrees of accuracy and to be applicable to many different systems. The book Viscous Fluid Flows by White [6] contains information on a large number of these solution methods.

Further advances in boundary layer analysis were made in 1938 by Von Karman and Tsien when integral forms of the boundary layer equations were used to analyze control volumes containing the boundary layer [10]. Solving a boundary layer using the integral form of the equations leads to a more general analysis method allowing for analysis of both turbulent and laminar flows. Analyzing the energy equation for the boundary layer using integration leads to a general equation for heat flux evaluated at the surface of the wall which is summarized by Equation 1.5.

$$q_w = k\left(\frac{\partial T}{\partial y}\right)_w \tag{1.5}$$

This equation leads to an important insight concerning the differences in heat flux for laminar and turbulent boundary layers. From studies of turbulence it is known that turbulent flows mix and interact at a higher rate than an equivalent laminar flow [1][5]. This higher rate of interaction leads to a shorter distance being needed to satisfy the wall boundary conditions creating higher gradients and leading to higher magnitudes of shear and heat flux at the wall in turbulent flows [5].

As higher flight speeds continued to emerge in fluid mechanics and a broader range of flight conditions needed to be evaluated more approximate methods were introduced to analyze boundary layers and the heat flux stemming from them in a wider set of conditions. In 1956 methods to approximate heat flux in both laminar and turbulent high speed flows were introduced by Van Driest [11]. From use of both experimental data and previous work in fluid mechanics Van Driest further broke down the behavior of heat flux and derived estimates for the Stanton number, Reynolds analogy factor, and recovery factor across a wide range of flow conditions. This work provides a significant knowledge base useful for estimating heat flux in compressible flowfields with either laminar or turbulent boundary layers for flat plates and stagnation points but does not give results for more complex geometries. Many approximate methods to calculate heat flux for high speed flight have been developed over the years which are documented by DeJarnette, Hamilton, Weilmuenster, and Cheatwood in [12].

The latest advances in heat flux modeling were introduced in 1986 when CFD simulations were used to model the flowfield around a full vehicle for the first time [13]. In this work Shang and Scherr used CFD simulations to model the aerodynamics and heat flux on a hypersonic aircraft during re-entry obtaining solutions with good agreement to experimental data [14]. Using CFD simulations to model aerodynamic effects provides a large number of advantages over the previously discussed methods. Unlike the approximate methods CFD simulations allow fully 3D flowfields around complex geometries to be analyzed while making few assumptions to the underlying equations [15]. The lack of assumptions to the Navier Stokes equations also increases the fidelity of solutions achieved from CFD since the full set of equations are applied throughout the flowfield being simulated [4].

Modern advances in digital computing have only increased the usefulness of CFD simulations allowing larger and more complex simulations to be performed than ever before [15]. The advances in computing power have also been further supported by research on CFD and the development of higher fidelity turbulence models, more powerful solution algorithms covering a broad range of applications, and more accurate numerical methods reducing errors and numerical dissipation [16]. The diverse toolset available in modern CFD codes allows for high fidelity heat flux calculations to be performed rapidly using parallelized computing which is utilized heavily for this work.

1.3 Research Objectives

The objective of this research is to implement a set of CFD simulations to calculate heat flux values near the fairing and payload bay for the BOLT-II flight test in support of thermal protection (TPS) calculations at CUBRC and JHAPL. The research presented will use multiple critical points identified along the simulated trajectory to simulate flight accurate heat flux in the CFD simulations performed. Data from this analysis describing the magnitude and distribution of heat flux expected in flight will be used in conjunction with data from JHAPL in support of vehicle design efforts at CUBRC. These results are being used to ensure a 30% factor of safety for thermal protection on the BOLT-II flight vehicle allowing it to survive the thermal loads that will be encountered during hypersonic flight.

2. METHODOLOGY

2.1 Simulation Geometry

The geometry modeled for the CFD simulations being performed was intentionally shortened from the full flight vehicle to account for known information and to improve the computational efficiency of the simulations. Government partners on the BOLT-II flight test have previously identified the necessary thermal performance characteristics of the second stage TU-758 Malemute rocket making its inclusion in the simulation geometry unnecessary. Additionally since the Navier-Stokes equations are hyperbolic above Mach 1 removing a downstream component of the flight vehicle will not affect any upstream part of the solution. Because of this it was determined that the simulation geometry only needed to include the BOLT-II flight test vehicle, the BOLT-II fairing, and the payload bay as seen in Figure 1.3.

2.2 Computational Toolbox

2.2.1 US3D

The US3D software is a CFD code developed by professor Graham Candler's research group at the University of Minnesota. This CFD solver is completely parallelized and offers a diverse toolset for accurately analyzing high speed flowfields on complex geometries [17]. For the purpose of predicting turbulent effects on the BOLT-II geometry the US3D CFD solver is desirable to use due to its ability to use many different solvers with low amounts of numerical dissipation and its ability to easily tailor the solver properties to fit each simulation.

The solvers used in US3D for these simulations were chosen to accurately and efficiently simulate the physics relevant to the turbulent heat flux being simulated. Since the free stream conditions being considered exist in the lower portion of the hypersonic speed regime the flow can still be considered to not be chemically reactive and therefore a perfect gas equation of state was implemented for these simulations. Iterations for the simulations were performed using implicit DPLR time integration on 6 sub-iterations with time steps determined based on user defined CFL numbers. For these simulations it was found to be advantageous for residual stability to ramp the CFL number smoothly from 0.08 to 1750 over the course of the first 6000 iterations. Inviscid fluxes were set to be 2nd order in space and were calculated using modified Steger-Warming flux vector splitting and 2nd order MUSCL flux extrapolation. For simulating turbulent effects a compressible Spalart-Allmaras turbulence model was used for the simulations. To address differences in heat flux values based on the turbulence model being used one simulation was also run a second time using a Menter SST turbulence model for comparison.

2.2.2 Pointwise

Pointwise is a mesh generation software specializing in CFD mesh generation. This mesh generation software offers a large variety of tools and element types that can be used for the definition and discretization of the control volume to be solved by a CFD code. Due to the level of detail needed to accurately simulate the flowfield around the regions of interest as well as the desire to have low numerical dissipation and short iteration times generating a structured mesh was determined to be the most ideal approach.

To work through generating a mesh for the simulations a two part iterative study was used to tailor both the wall Y+ characteristics and the grid convergence based on wall heat flux. Since all free stream conditions being run for the study were in the hypersonic speed regime the outer boundary of the control volume being meshed was chosen to closely follow the shock coming off of a quarter-symmetry geometry at Mach 5 and $Re/L = 40 \times 10^6 \frac{1}{m}$. The first part of the grid tailoring process involved tailoring the distribution and number of cells normal to the wall of the vehicle until a wall Y+ value of 1 or lower was achieved across the surface of the vehicle. From here a convergence study was run increasing the cell density of the mesh until the wall heat flux values on a steady state solution did not significantly change with further grid density at which point the grid was said to be converged. The converged mesh generated using these methods was used to simulate all of the free stream conditions used for the heating studies.

2.3 Simulation Conditions

For the CFD simulations run three of the free stream conditions were pulled from points identified along the flight trajectory representing the highest Mach numbers and the highest Reynolds numbers expected in flight during both ascent and descent. The fourth free stream condition used was a point of intense heat flux identified previously by industry partners along the BOLT-II flight trajectory at $Re/L = 35 \times 10^6 \frac{1}{m}$. From previous analyses an isothermal wall temperature of 450 K was chosen to be a reasonable condition for the heat transfer simulations being performed. For each simulation the free stream temperature was also chosen to be a constant at 220 Kelvin. This was done to eliminate free stream temperature as a variable affecting heat flux and to allow free stream conditions to be completely defined by a choice of Mach number and Reynolds number from the trajectory using Sutherland's Law for air and the definition of Reynolds number in Equation 2.1 and Equation 2.2 respectively.

$$\mu = \mu_0 \left(\frac{T}{T_0}\right)^{3/2} \left(\frac{T_0 + S}{T + S}\right) \tag{2.1}$$

$$\frac{Re}{L} = \frac{\rho_\infty M_\infty \sqrt{\gamma R T_\infty}}{\mu} \tag{2.2}$$

For the heating study performed a set of 20 CFD simulations were run. Free stream conditions calculated from the trajectory that were used for the heating simulations are summarized in Table 2.1. For each free stream condition listed in Table 2.1 a set of 5 angles of attack were simulated based off of the expected maximum angles seen in trajectory simulations. A summary of these angles of attack is listed in Table 2.2. For the angles of attack and conditions of each simulation the velocity components of the free stream in 3D space are described by Equation 2.3.

$\frac{Re}{L}\left[\frac{1}{m}\right]$	M_∞	p_∞ [Pa]	$\rho_\infty \left[\frac{kg}{m^3}\right]$	T_∞ [K]	T_w [K]
40×10^6	5.10	23984	0.380	220	450
35×10^6	5.14	20848	0.330	220	450
20×10^6	5.70	10730	0.169	220	450
15×10^6	6.00	7645	0.121	220	450

Table 2.1: Free stream conditions for heat flux simulations

Condition	α [deg.]	β [deg.]
1	0	0
2	2	0
3	4	0
4	0	2
5	0	4

Table 2.2: Angles of attack applied to free stream conditions

$$\begin{bmatrix} u \\ v \\ w \end{bmatrix} = U_\infty \begin{bmatrix} \cos(\alpha)\cos(\beta) \\ \sin(\alpha)\cos(\beta) \\ -\sin(\beta) \end{bmatrix} \tag{2.3}$$

In addition to these simulation one additional simulation was run to investigate the dependence of the results on the turbulence model being used. For the turbulence model dependence simulation the condition of $Re/L = 35\times10^6\frac{1}{m}$ and $\alpha = 4^\circ$ was used and all solver settings were kept constant besides the turbulence model which was switched from compressible Spalart-Allmaras to Menter

SST. The difference between heat flux values measured was calculated using Equation 2.4.

$$\%Difference = \frac{(q_w)_{SpalartAllmaras} - (q_w)_{MenterSST}}{(q_w)_{SpalartAllmaras}} \times 100\% \tag{2.4}$$

2.4 Wind Tunnel Tests

To further model the flow characteristics and patterns of heat flux near the fairing and payload bay wind tunnel tests were conducted on a 25% scale model of the flight geometry. The wind tunnel model used for these tests was manufactured on a 3D printer from polycarbonate material and included the BOLT-II flight vehicle, the fairing, the conical transition of the payload bay, and a small length of the cylindrical section of the payload bay. The wind tunnel model can be seen in Figure 2.1.

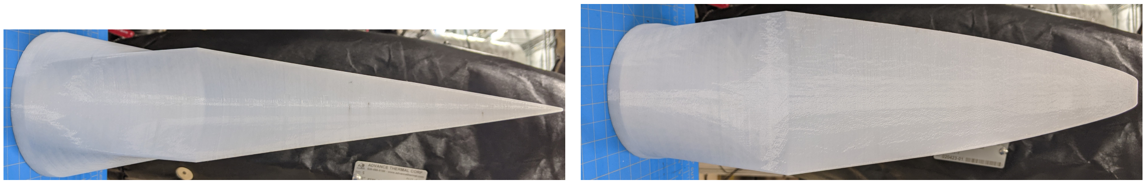

(a) Side view

(b) Top view

Figure 2.1: Wind tunnel model of the BOLT-II flight configuration

Wind tunnel tests on this model were conduced in the Actively Controlled Expansion (ACE) wind tunnel. ACE is a conventional wind tunnel with the ability to vary Mach numbers by manually adjusting the height of the nozzle throat [18]. The test section of ACE is 0.69 meters long and has a cross section 0.23 meters in width with a height of 0.36 meters. A diagram of the ACE wind tunnel can be seen in Figure 2.2 which is reprinted from [19].

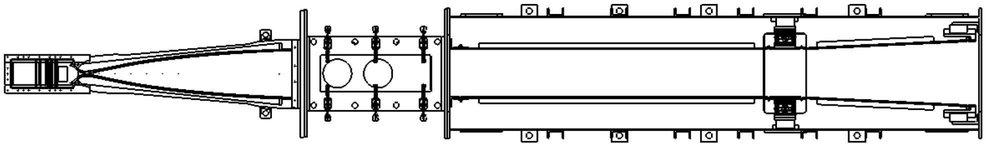

Figure 2.2: Diagram of the ACE wind tunnel (reprinted from [19])

To obtain heat flux data in wind tunnel tests infrared thermography was conducted using a FLIR SC8100 camera. The raw data describing time histories of the surface temperatures on the model was analyzed in MATLAB using the NAL 1D heat flux code. This code was developed to post process IR images from wind tunnel tests for the HIFiRE-5 flight test [20]. The code was modified for use with the BOLT-I flight test and is also being used in wind tunnel tests for the BOLT-II flight test [21].

For the 1D heat flux code data of temperature at the surface for each time step is known from the IR camera. For a 1D temperature profile Equation 2.5 explains the time transient behavior that will occur. In the code a constant thickness of material is assumed and this length of material is discretized spatially. Using a 1st order forward finite difference for time and a 2nd order central finite difference for the spatial component the temperature at each point within the material can be propagated forward in time using Equation 2.6 with the thermal diffusivity being described by Equation 2.7.

$$\frac{\partial T}{\partial t} = \xi \frac{\partial^2 T}{\partial x^2} \tag{2.5}$$

$$\frac{T_j^{i+1} - 2T_j^i}{\Delta t} = \xi \frac{T_{j+1}^i - T_j^i + T_{j-1}^i}{\Delta x^2} \tag{2.6}$$

$$\xi = \frac{k}{\rho c_p} \tag{2.7}$$

For these equations the superscript i denotes the time step of each variable and the subscript j denotes the spatial position of each variable relative to the current time step and spatial point being analyzed respectively. At each time step the boundary condition applied is that the temperature at the wall is the temperature from the IR image at that time step and the initial temperature distribution at the first time step is isothermal across each 1D cross section. Heat flux to the wall is calculated at each time step using the temperature profile and a 2 point forward finite difference seen in Equation 2.8. Material properties for the polycarbonate used in these calculations are listed in Table 2.3.

$$q_w = k\frac{3T_w^i - 2T_{w+1}^i + T_{w+2}^i}{2\Delta x} \tag{2.8}$$

Material	$k\ [\frac{W}{m^2K}]$	$c_p\ [\frac{J}{kgK}]$	$\rho\ [\frac{kg}{m^3}]$
Polycarbonate	0.19	1200	1200

Table 2.3: Material properties of polycarbonate used in the 1D heat flux code

For the wind tunnel tests performed a Mach number of 5.7 was used to allow for comparisons with the set of CFD simulations run at the same Mach number. Comparisons between the heat flux characteristics in wind tunnel testing and CFD simulations were used to characterize the validity of CFD data obtained from this study.

Because the flight conditions and scales being used for CFD simulations are drastically different than the wind tunnel conditions the magnitudes of heat flux obtained from the two are not directly comparable. To resolve this problem one additional CFD simulation was run at ACE wind tunnel conditions with a 25% scale version of the heating study mesh being used to match the 25% scale wind tunnel model. The conditions run for this simulation are summarized in Table 2.4.

$\frac{Re}{L}\left[\frac{1}{m}\right]$	M_∞	$U_\infty\left[\frac{m}{s}\right]$	p_∞ [Pa]	$\rho_\infty\left[\frac{kg}{m^3}\right]$	T_∞ [K]	T_w [K]
6.5×10^6	5.70	870.1	477	0.0285	58	300

Table 2.4: CFD conditions used to simulate the ACE wind tunnel

Free stream conditions used in this simulation were obtained from data recorded by the ACE wind tunnel sensor array during the wind tunnel tests. The wall temperature of 300 K was chosen to match the approximate initial temperature of the model during the wind tunnel test and has been used in previous works by industry partners to simulate wind tunnel conditions [22]. To resolve the differences between the isothermal wall temperature in CFD and the variable wall temperature in wind tunnel tests the Stanton number was used for comparison in place of dimensional heat flux. The Stanton number was calculated for both CFD and wind tunnel tests using Equation 2.9 where T_{aw} is the adiabatic wall temperature which was calculated using Equation 2.10. Wind tunnel conditions used in these calculations are listed in Table 2.5.

$$St = \frac{q_w}{\rho_\infty U_\infty c_p (T_{aw} - T_w)} \tag{2.9}$$

$$T_{aw} = T_\infty\left(1 + \frac{\gamma - 1}{2} M_\infty^2\right) \tag{2.10}$$

$\frac{Re}{L}\left[\frac{1}{m}\right]$	M_∞	T_∞ [K]	$\rho_\infty\left[\frac{kg}{m^3}\right]$	$U_\infty\left[\frac{m}{s}\right]$	T_{aw} [K]
6.5×10^6	5.69	58	0.0285	867.4	432.4

Table 2.5: ACE wind tunnel conditions used for calculations

3. RESULTS

3.1 Grid Convergence Study

In the process of generating a converged mesh for the heat flux simulations it was found that the wall spacing needed to achieve Y+ values near 1 ended up being significantly smaller than expected. The Y+ numbers tended to be significantly larger around the fairing and payload transition and a wall spacing of 1×10^{-8} meters with 200 cells in the wall normal direction was required universally to achieve low enough Y+ values in these simulations as seen in Figure 3.1.

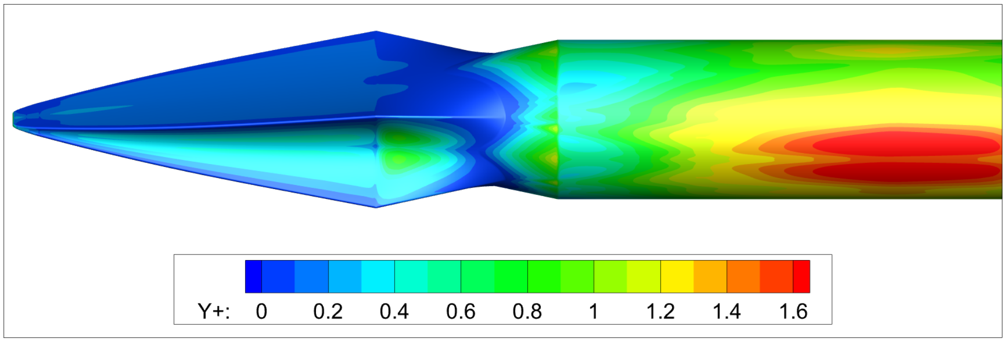

Figure 3.1: Wall Y+ values on final mesh at $Re/L = 40 \times 10^6 \frac{1}{m}$

The cell density of the quarter symmetry grid was also found to produce grid converged wall heat flux with around 15 million cells as seen in Figure 3.2. The wall heat flux values in the test simulations showed insignificant change between 15 million and 30 million cells. The 15 million cell mesh that was generated using this process was therefore deemed to be significantly grid converged and capable of accurately resolving the flowfields being investigated. This grid was used for all subsequent heating simulations performed and was mirrored across the necessary symmetry planes to handle angles of attack.

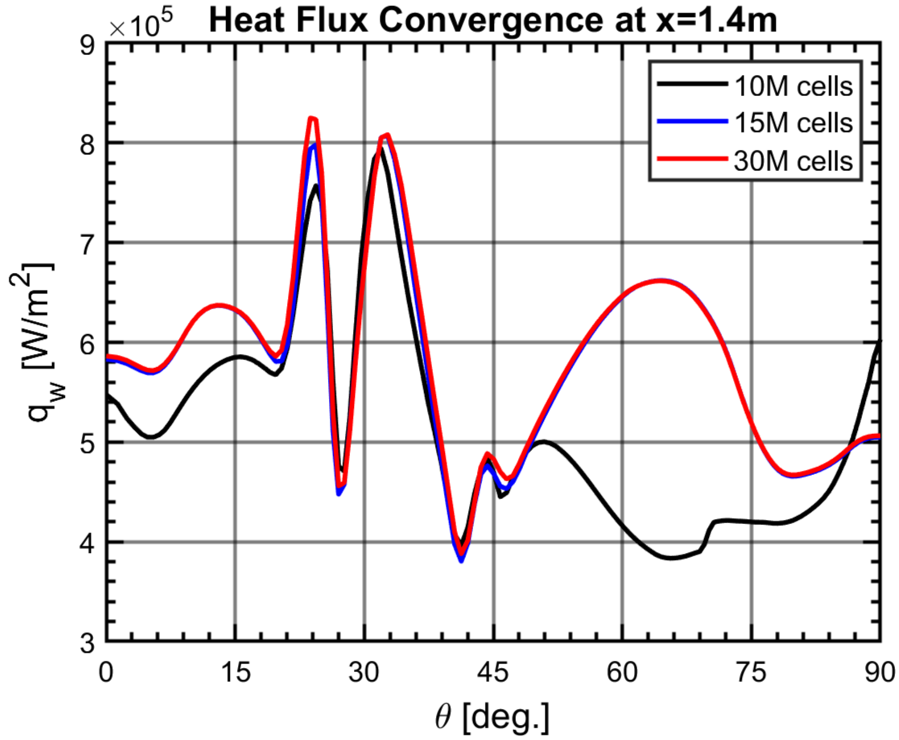

Figure 3.2: Convergence of heat flux with grid density

3.2 Heating Study

From the simulations that were run a common pattern was observed for the locations of maximum heat flux. The heat flux pattern shown in Figure 3.3 is very similar to the heat flux observed in all of the cases investigated and will be used to point out details and major features of the emergent behavior.

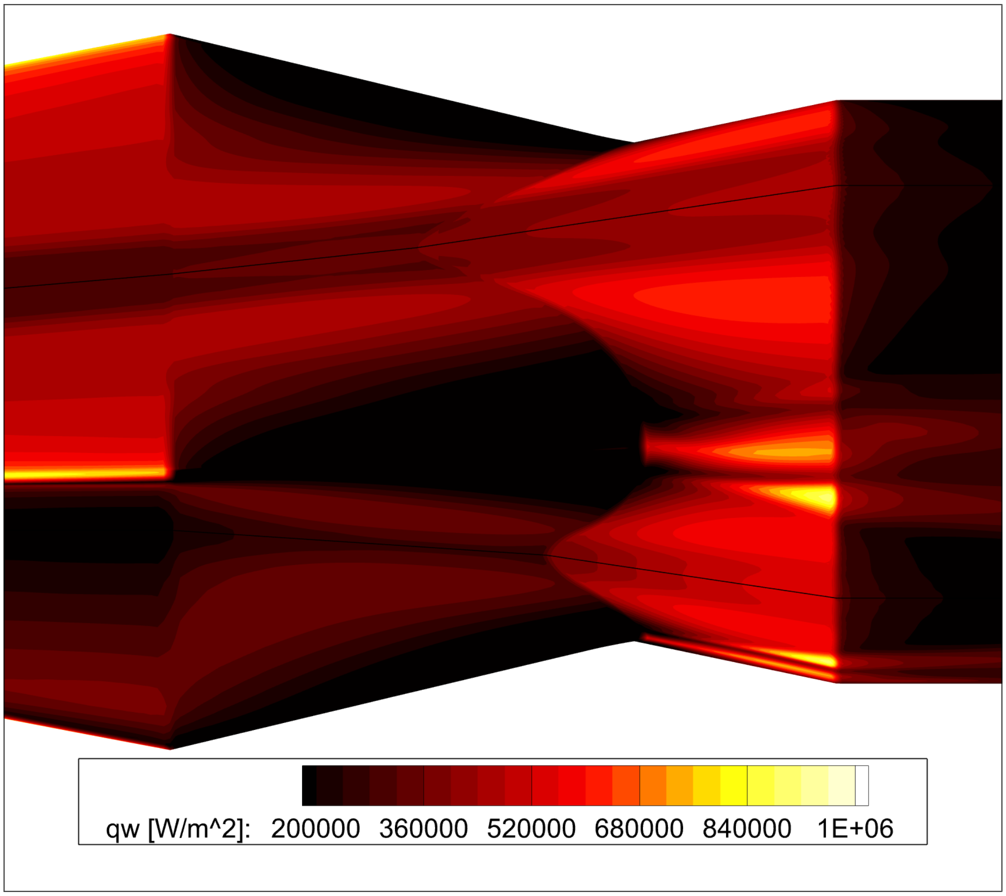

Figure 3.3: Heat flux at $Re/L = 35 \times 10^6 \frac{1}{m}$ and $\alpha = \beta = 0$

On the BOLT-II fairing two areas of high heat flux exist, one in the gutter region and the other just behind the test surface. These two areas of high heat flux on the fairing exist in all simulations that were run with the area behind the test surface always having a higher magnitude of heat flux than the area behind the gutter. On the payload bay the region with the highest heat flux was always at the end of the conical transition just above and below the low radius curves of the fairing. While this one spot of the payload bay experiences the most intense heat flux it is worth noting that a large proportion of the conical transition experiences high heat flux as well. On the cylindrical portion of the payload bay behind these regions heat flux was always found to be much less significant.

As the angle of attack increases in α the free stream becomes more incident to the test surface on the -Y side of the vehicle. The flow being more incident to this surface causes an increase in heat transfer on the -Y side of the geometry which can be seen in Figure 3.4.

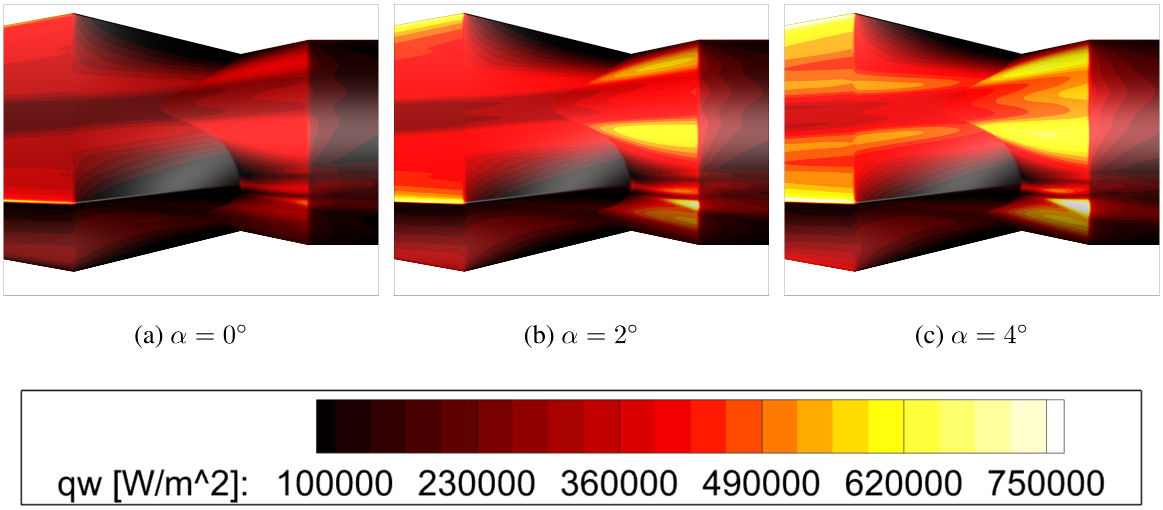
(a) $\alpha = 0°$

(b) $\alpha = 2°$

(c) $\alpha = 4°$

Figure 3.4: Heat flux evolving in α at $Re/L = 15 \times 10^6 \frac{1}{m}$

As the angle of attack increases not only does the heat flux increase on incident surfaces but it also increases significantly at the lower of the two spots on the payload bay. To understand why this heat flux spot on the payload bay increases so significantly with α the reason the spot exists must be investigated. Further observation of the flow characteristics close to this region reveal that as flow crosses the end of the BOLT-II flight vehicle the boundary layer that was previously running along the leading edge rapidly expands as it moves along the fairing as seen in Figure 3.5. Streamlines coming directly from the leading edge at the end of BOLT-II then flow until they interact with the conical section of the payload bay in the area of these max heat flux spots which is shown in Figure 3.6.

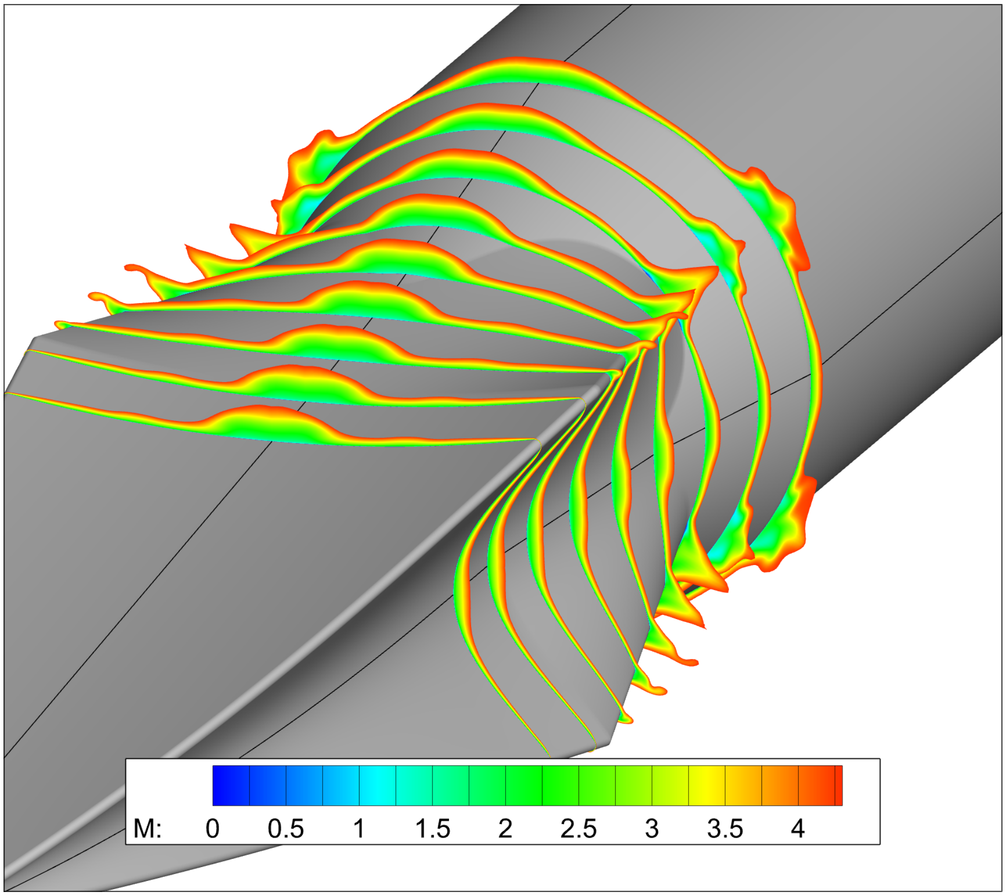

Figure 3.5: Boundary layer expansion along payload for $\alpha = \beta = 0$ and $Re/L = 20 \times 10^6 \frac{1}{m}$

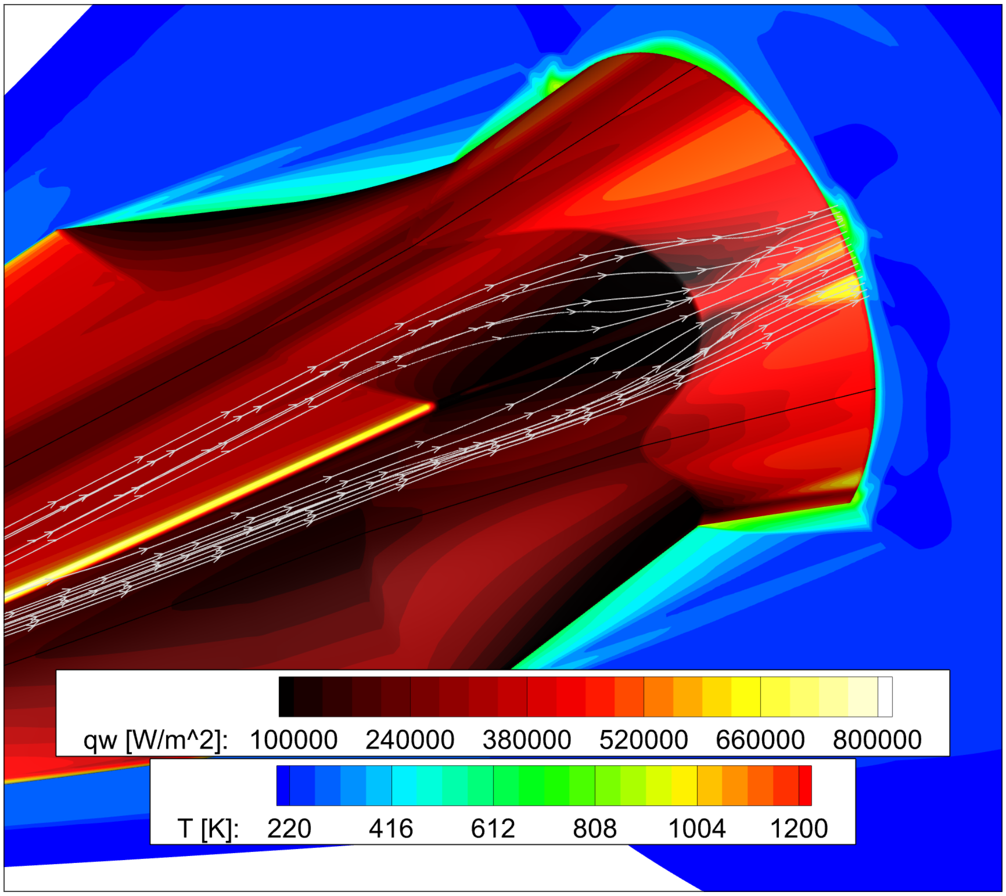

Figure 3.6: Leading edge streamline propagation for $\alpha = \beta = 0$ and $Re/L = 20 \times 10^6 \frac{1}{m}$

The streamlines coming off of this leading edge are part of a wingtip vorticy which is caused by the deflection imparted to the fluid by the vehicle. The vorticity coming from this leading edge interacts with the payload bay and causes the area of intense heat flux that is observed. This also explains why angles of attack in α cause significant increases in heat flux at that point. When at an angle of attack the vehicle imparts a greater deflection on the fluid increasing the vorticity generated on the leading edge that can act on the payload bay. This can be seen as the streamlines in Figure 3.7 deforming more severely with increasing α and by the increased expansion of the boundary layer with increasing α shown in Figure 3.8.

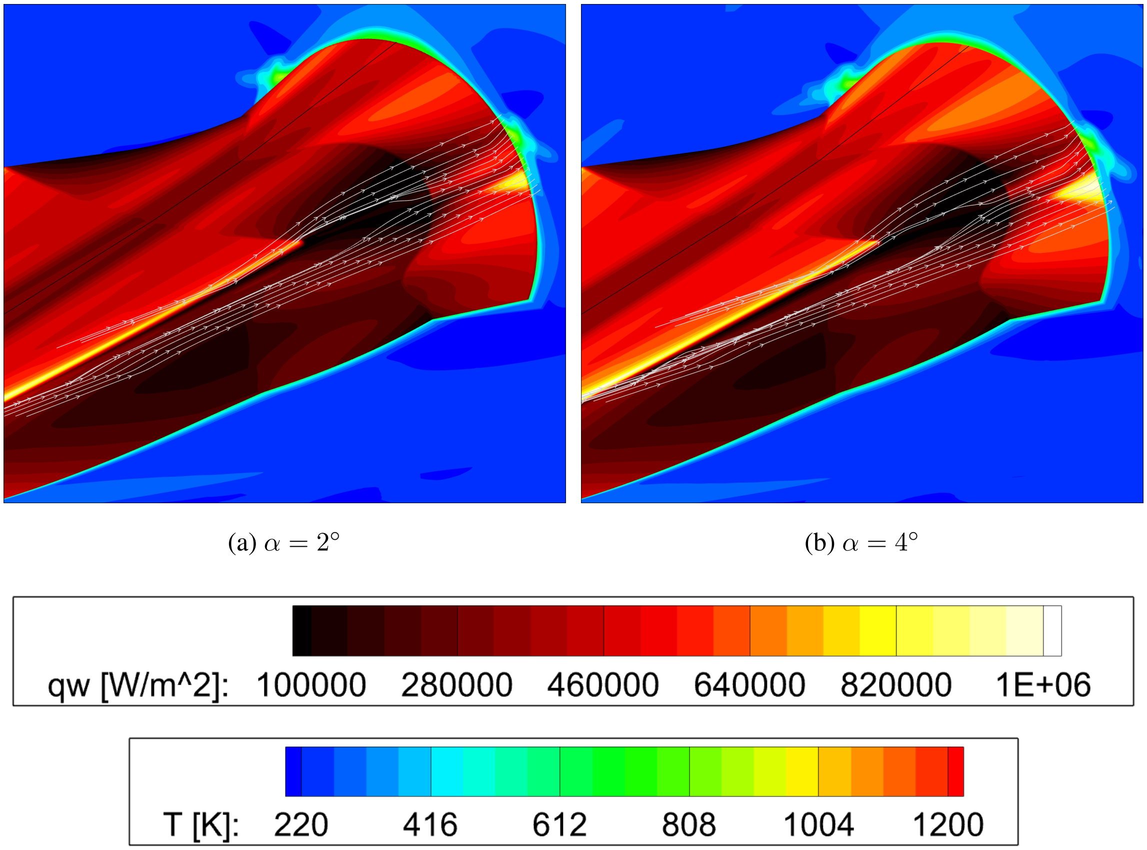
(a) $\alpha = 2°$

(b) $\alpha = 4°$

Figure 3.7: Streamline propagation in α for $Re/L = 20 \times 10^6 \frac{1}{m}$

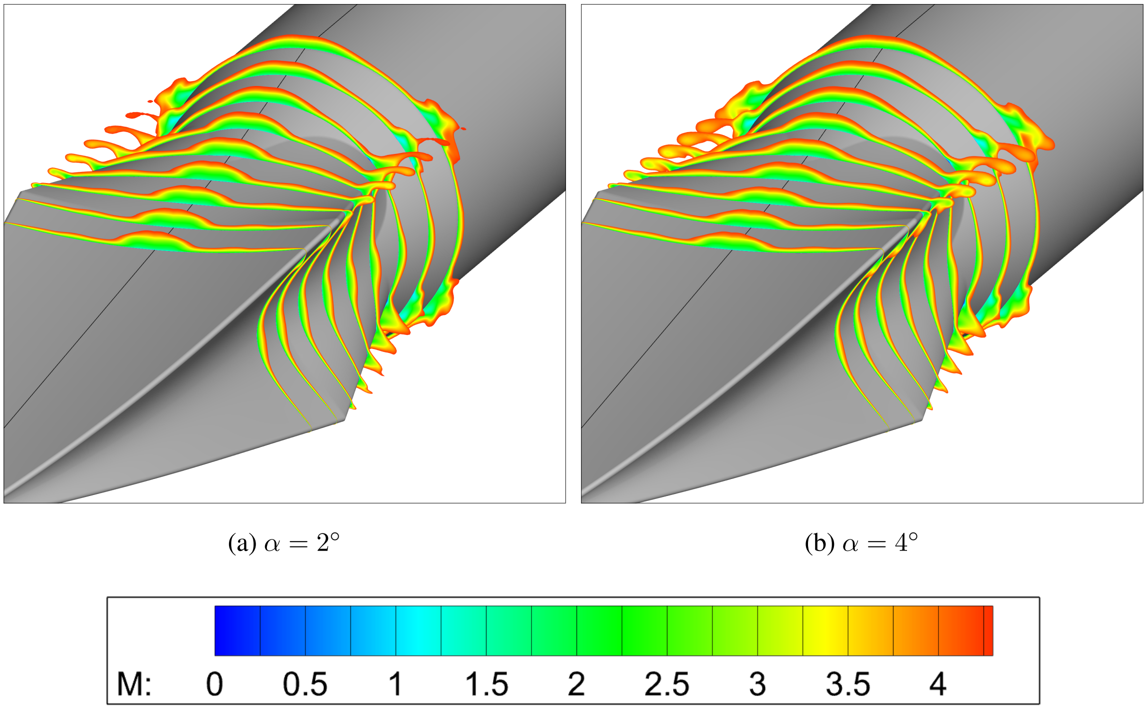

(a) $\alpha = 2°$

(b) $\alpha = 4°$

Figure 3.8: Boundary layer expansion in α for $Re/L = 20 \times 10^6 \frac{1}{m}$

As the angle of attack increases in β the free stream becomes more incident to the gutter causing an increase in the magnitude of heat flux in the gutter and causing flow features on the test surface to shift off center as can be seen in Figure 3.9.

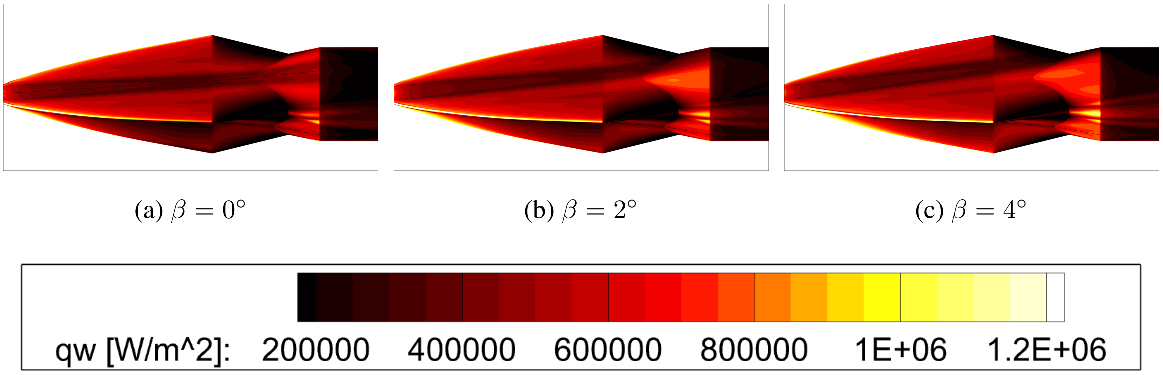

(a) $\beta = 0°$

(b) $\beta = 2°$

(c) $\beta = 4°$

Figure 3.9: Heat flux evolving in β at $Re/L = 40 \times 10^6 \frac{1}{m}$

With a portion of the flow being incident to the gutter the values of heat flux measured in the fairing's gutter came close to those measured on the fairing behind the test surface but never surpassed them. As β increases the payload's max heat flux spot also exhibits a slight behavioral change. In Figure 3.3 it is observed that the spot of maximum heat flux on the payload is broken up into an upper spot and a lower spot which are closer to the test surface and gutter respectively. So far each max heat flux measurement on the payload has been on the lower of these two spots but for simulations at $\beta = 4°$ the maximum heat flux occurs at the upper spot. This change can be seen as β progresses in Figure 3.10.

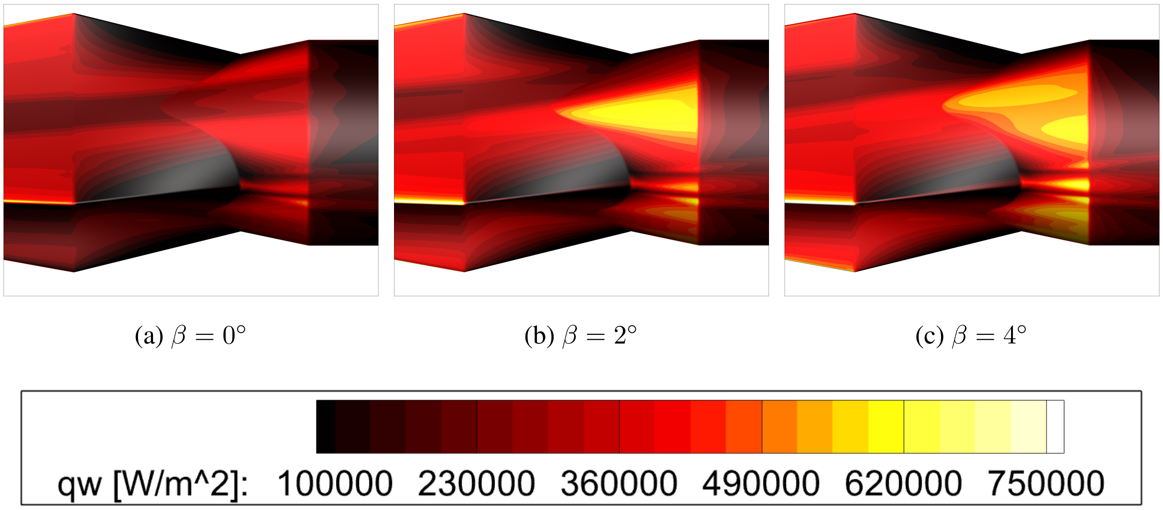
(a) $\beta = 0°$ (b) $\beta = 2°$ (c) $\beta = 4°$

Figure 3.10: Heat flux evolving in β at $Re/L = 15 \times 10^6 \frac{1}{m}$

As β increases flow from the gutter is increasingly pushed in the -Z direction due to the component of the free stream incident to the gutter. At $\beta = 4°$ this incident component is strong enough to cause flow to jump over the low radius edge of the fairing as seen in Figure 3.11. Similar to the previously described mechanisms for α this deflection of streamlines with increasing β creates vorticity which interacts with the payload on the upper of the two max heat flux points. This interaction is what causes the switch in behavior making the upper spot have a higher magnitude of heat flux.

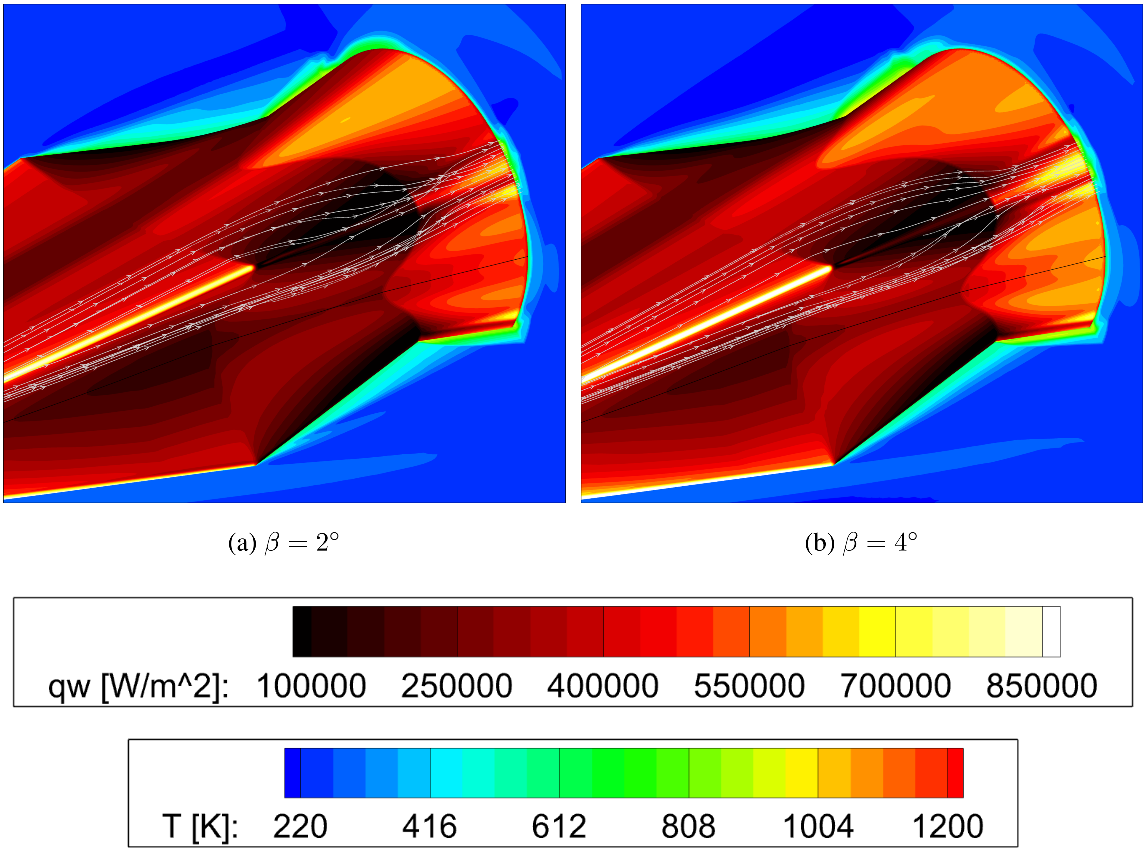
(a) $\beta = 2°$

(b) $\beta = 4°$

Figure 3.11: Streamline propagation in β for $Re/L = 20 \times 10^6 \frac{1}{m}$

The maximum heat flux magnitude expected in flight, for the four free stream conditions tested, was found on both the fairing and the payload bay. Heat flux values for the fairing can be found in Figure 3.12 and heat flux values for the payload bay can be found in Figure 3.13.

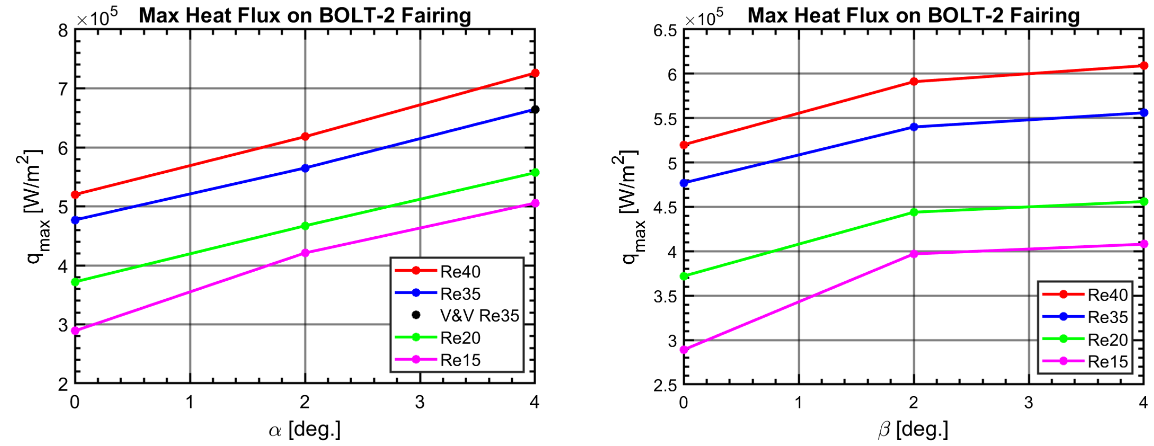

(a) Fairing α

(b) Fairing β

Figure 3.12: Maximum heat flux values on the fairing

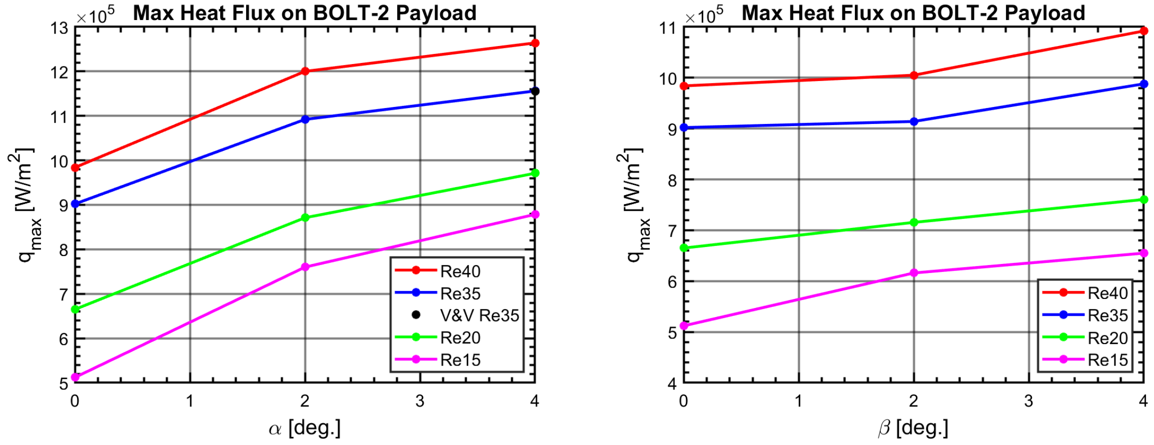

(a) Payload bay α

(b) Payload bay β

Figure 3.13: Maximum heat flux values on the payload bay

To assess the dependency of these predictions on the turbulence model being used the simulation for $Re/L = 35 \times 10^6 \frac{1}{m}$ at $\alpha = 4^\circ$ was simulated a second time using the Menter SST turbulence model but keeping every other setting the same. As seen in Figure 3.14 the solutions generated by the simulations are nearly identical. The maximum heat flux values from the solution to this simulation are also recorded in Figure 3.12 and Figure 3.13 and both have less than a 0.1% difference from the corresponding value found using Spalart-Allmaras.

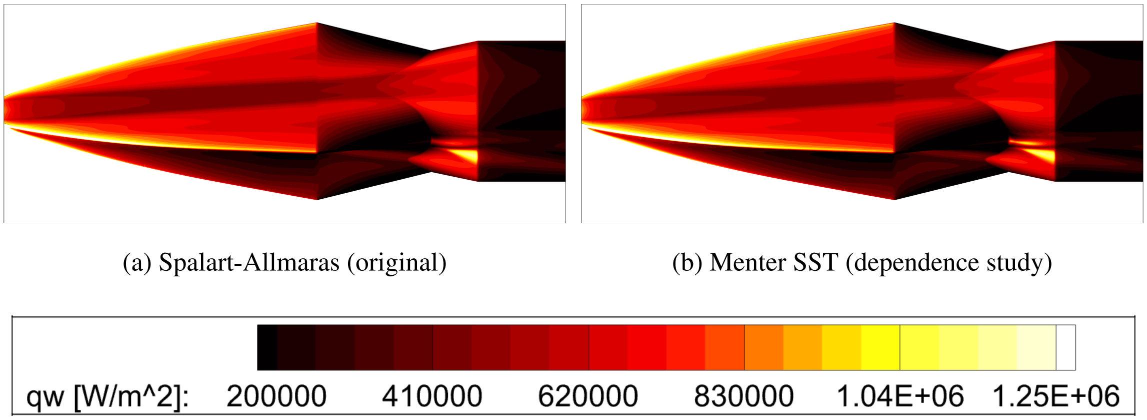

(a) Spalart-Allmaras (original)

(b) Menter SST (dependence study)

Figure 3.14: Cases from the turbulence model independence study

3.3 Heating Study Verification

Data from the wind tunnel tests performed was post processed to show heat flux on the surface of the model. Comparing the patterns of heat flux observed in wind tunnel tests to the patterns of heat flux in steady state CFD simulations similar overall behavior can be observed.

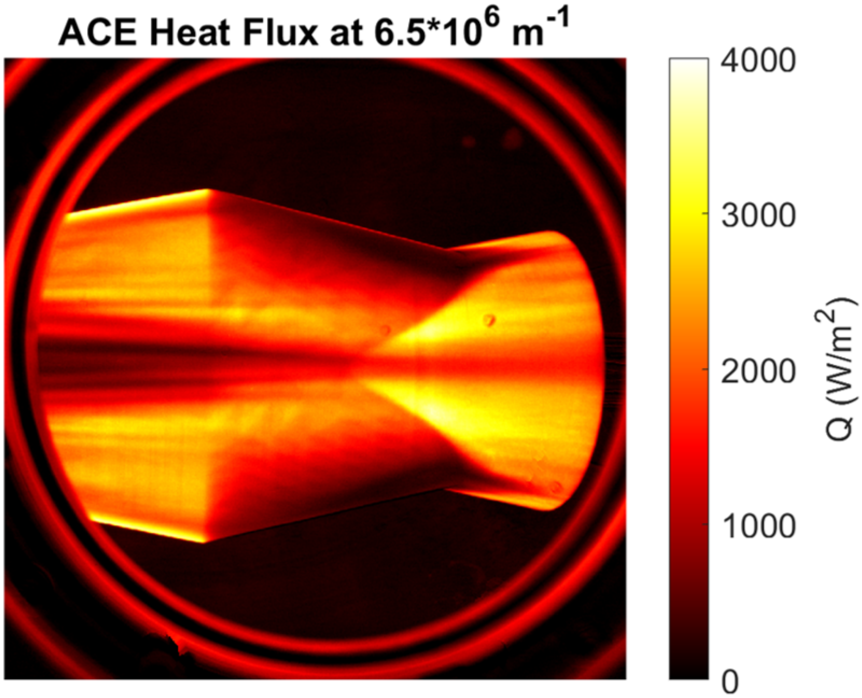

Figure 3.15: Test surface view of ACE wind tunnel test heat flux

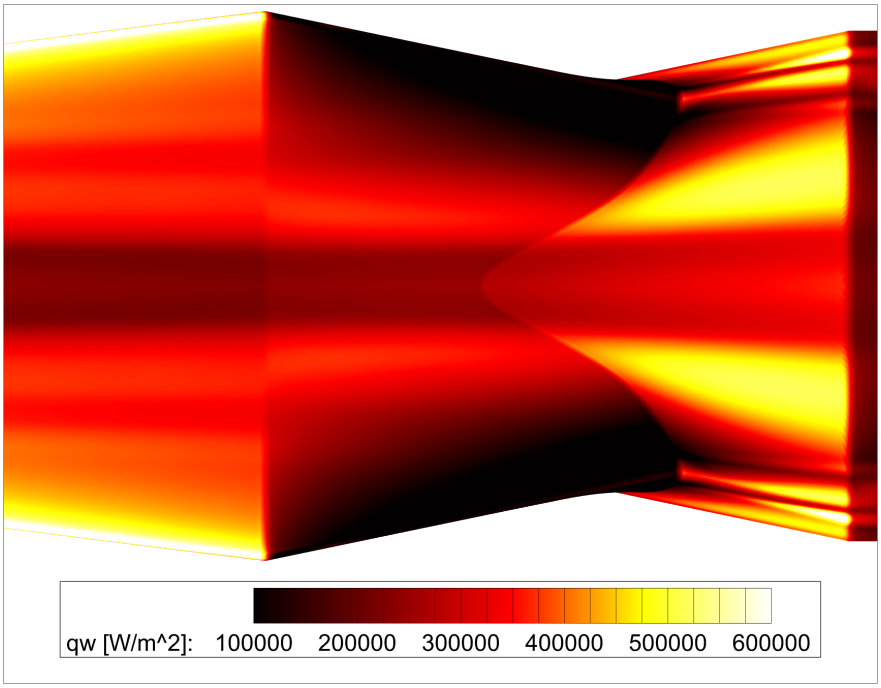

Figure 3.16: Test surface view of CFD heat flux at $Re/L = 20 \times 10^6 \frac{1}{m}$

The heat flux seen behind the BOLT-II test surface in wind tunnel data exhibited patterns similar to those in CFD which can be seen in Figure 3.15 and Figure 3.16 respectively. On the fairing directly behind the test surface the region of maximum heat flux is slightly offset from the centerline which is the same behavior observed in CFD. On the conical section of the payload bay the heat flux also seems to behave as predicted by the CFD simulation forming a wedge of higher magnitude heat flux slightly offset from the lower magnitude median.

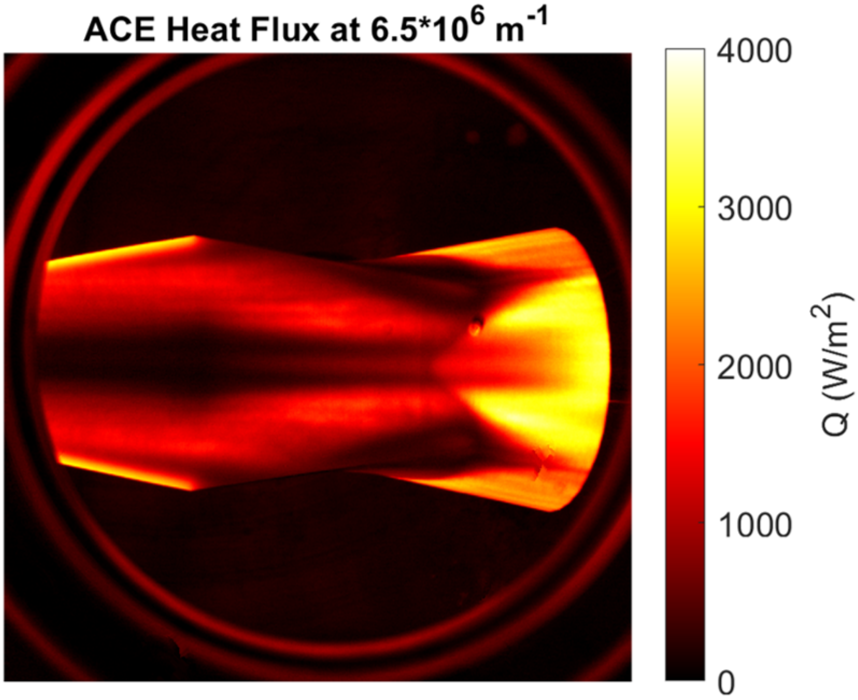

Figure 3.17: Gutter view of ACE wind tunnel test heat flux

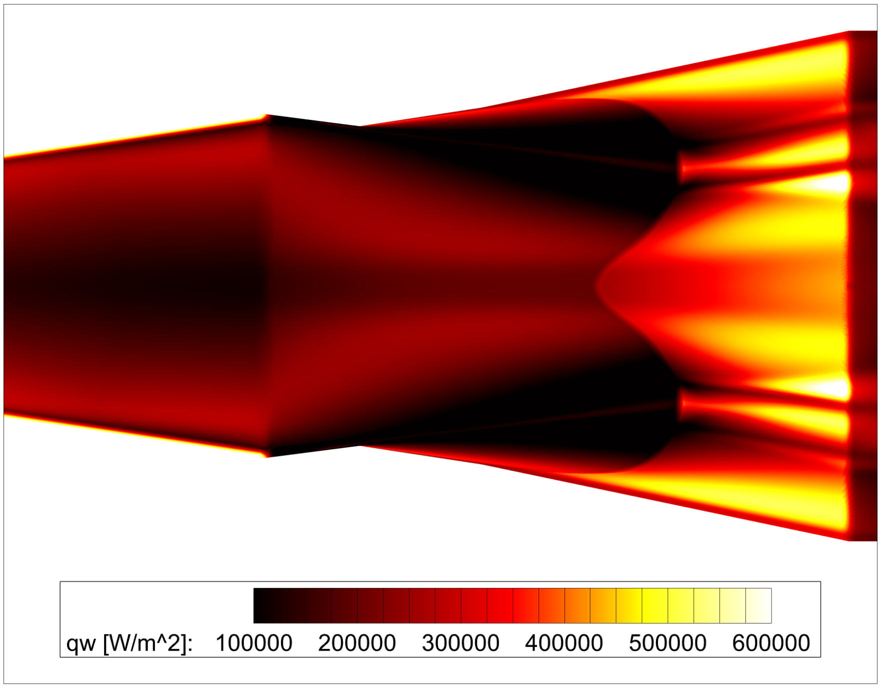

Figure 3.18: Gutter view of CFD heat flux at $Re/L = 20 \times 10^6 \frac{1}{m}$

The heat flux patterns observed behind the BOLT-II gutter in wind tunnel testing and CFD are shown in Figure 3.17 and Figure 3.18 respectively. The heat flux pattern in wind tunnel tests on the fairing directly behind the flight test vehicle is extremely similar to that seen in CFD simulations with lower heat flux along the center-line and a wedge of heat flux avoiding the low radius curve separating the gutter and test surface. Unlike the figures of heat flux from CFD simulations the patterns of heat flux observed on the payload bay's conical transition in wind tunnel tests did not exhibit as distinct of a separation between features and instead the heat flux features tended to blend together as seen in Figure 3.17. Further into the wind tunnel run at a Reynolds number of $\frac{Re}{L} = 6.9 \times 10^6 \frac{1}{m}$ these heat flux features did become slightly more distinct and can be seen in Figure 3.19.

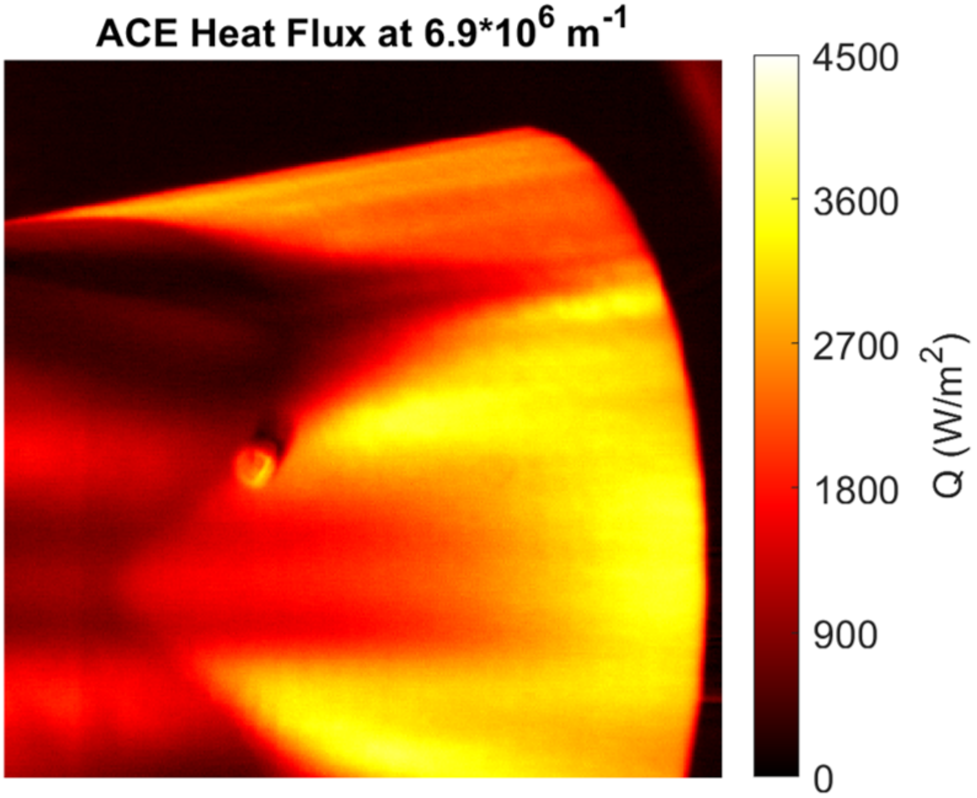

Figure 3.19: ACE wind tunnel test heat flux zoomed in on payload bay

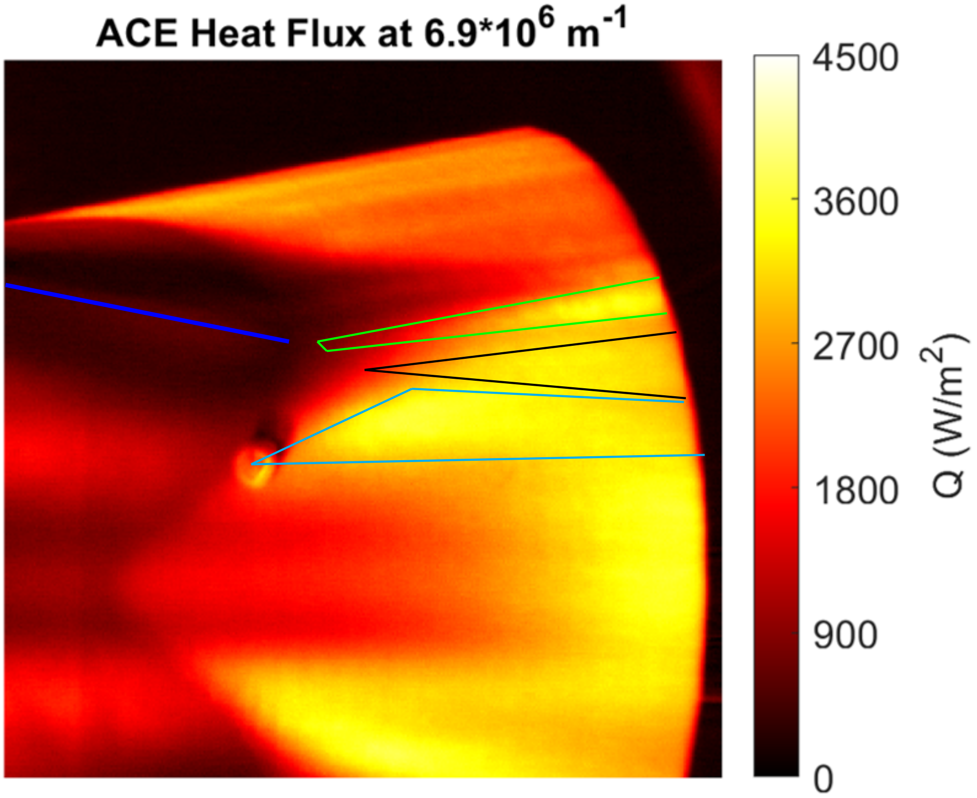

Figure 3.20: Major heat flux features from ACE wind tunnel testing

To further separate the heat flux features identified important features have been color coded in Figure 3.20. The first feature to see is the upper vorticity interaction feature just behind the low radius edge of the fairing which is enclosed in green. This feature is separated from the other two features below it by a slightly decreased section of heat flux and directly follows the low radius edge which is identified by the blue line on the upper left. The other two features are the lower high heat flux feature and the off-median wedge which become much less distinct in the wind tunnel and blend together in heat flux results. The lower vorticity interaction feature, enclosed in black, and the off-median wedge, enclosed in cyan, were separated by a slight decrease in heat flux at the end of the model which is not easy to see. This slight decrease at the end can be followed in the -X direction to find the tip of the wedge at the beginning of the two features next to the tip of the black triangle enclosing it. Identifying the off-median wedge enclosed in cyan follows from the identification of the lower vorticity feature.

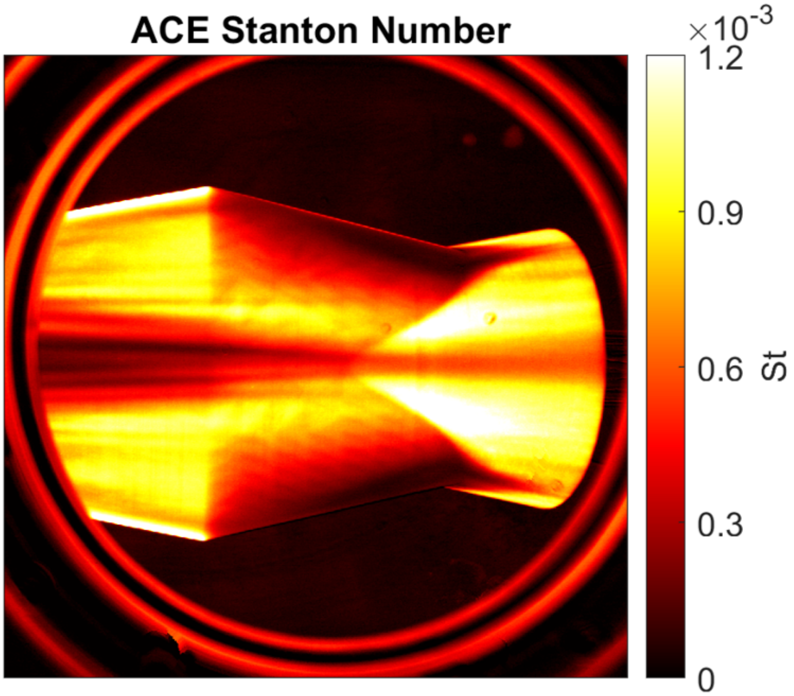

Figure 3.21: Test surface view of ACE wind tunnel Stanton number at $Re/L = 6.5 \times 10^6 \frac{1}{m}$

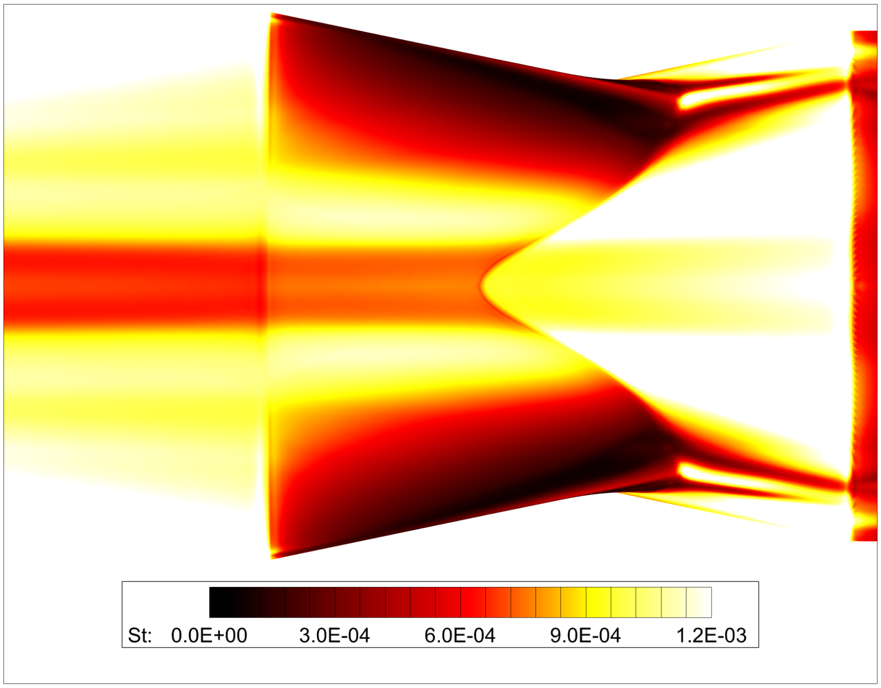

Figure 3.22: Test surface view of CFD Stanton number at ACE conditions

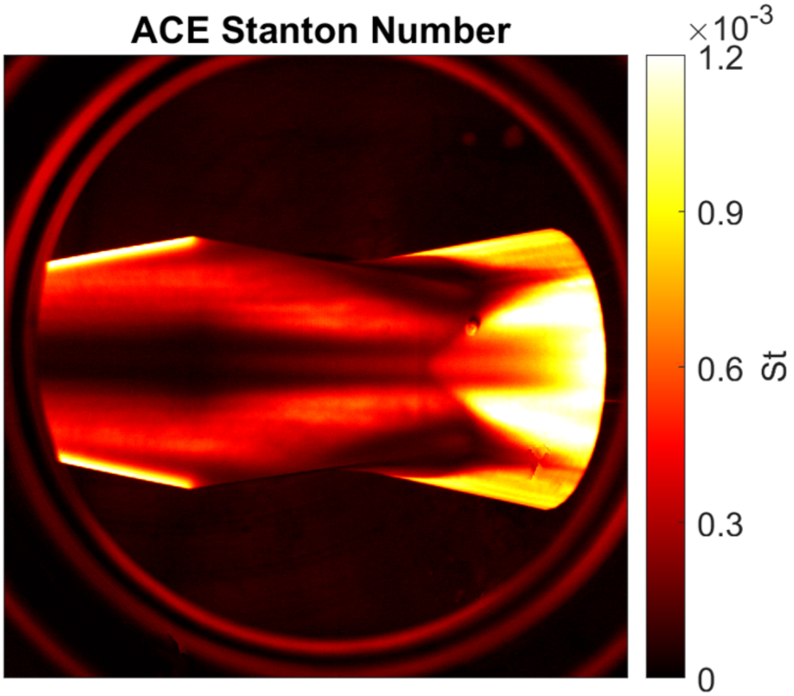

Figure 3.23: Gutter view of ACE wind tunnel Stanton number at $Re/L = 6.5 \times 10^6 \frac{1}{m}$

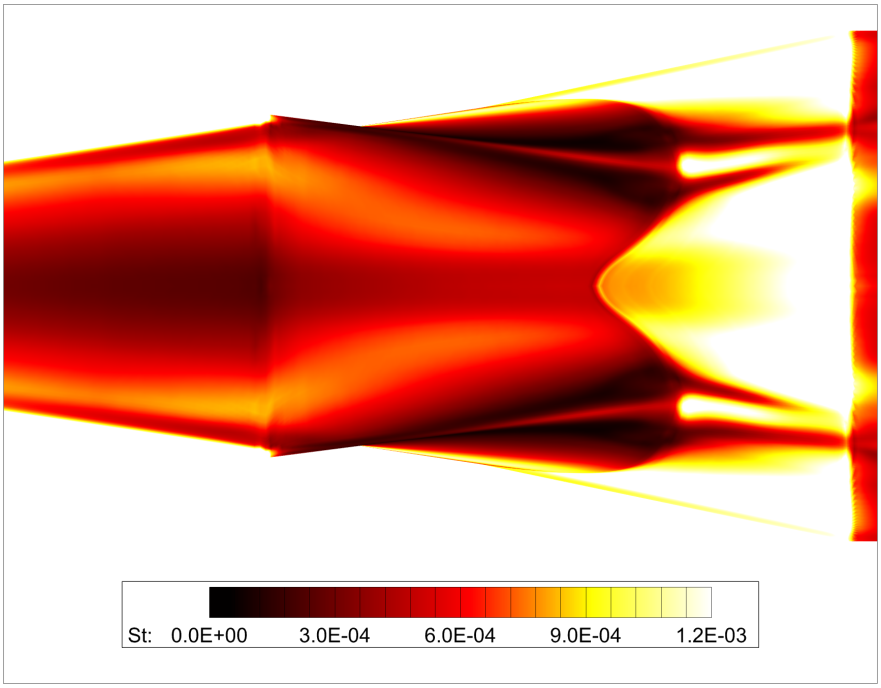

Figure 3.24: Gutter view of CFD Stanton number at ACE conditions

Stanton number data from ACE wind tunnel testing and the CFD simulation run at ACE conditions were similar in both pattern and magnitude however it was noted that the CFD simulation slightly over-predicted the magnitude of heat flux relative to wind tunnel data. It is also noted that CFD tends to propagate heat flux features further along the surface compared to wind tunnel tests. This propagation is especially apparent when observing the wedge of heat flux on the Y side of the conical transition just behind the fairing which dissipates and smooths out in wind tunnel tests, as observed in Figure 3.21, but extends across the transition in CFD results, shown in Figure 3.22. The gutter view of Stanton number for ACE results in Figure 3.23 and for CFD results in Figure 3.24 reveals that the lower Reynolds number in wind tunnel testing did have an effect on the heat flux features seen when compared to trajectory based conditions. These figures show agreement in the merging of the lower heat flux feature caused by leading edge vorticity and the off-median heat flux wedge at these lower Reynolds numbers.

While reviewing the results from wind tunnel tests two sources of error affecting the results were identified. The first source of error identified was that the wind tunnel tests were run at a slightly non-zero angle of attack but compared to CFD simulations with no angle of attack. For both wind tunnel runs shown heat flux features were slightly angled and slightly greater in magnitude on one side leading to the identification of this error. The second source of error identified is due to imperfections in the glass on the ACE wind tunnel which are circled in Figure 3.25. Due to optical phenomena affecting the IR camera the results of the heat flux code in the region of these imperfections are distorted.

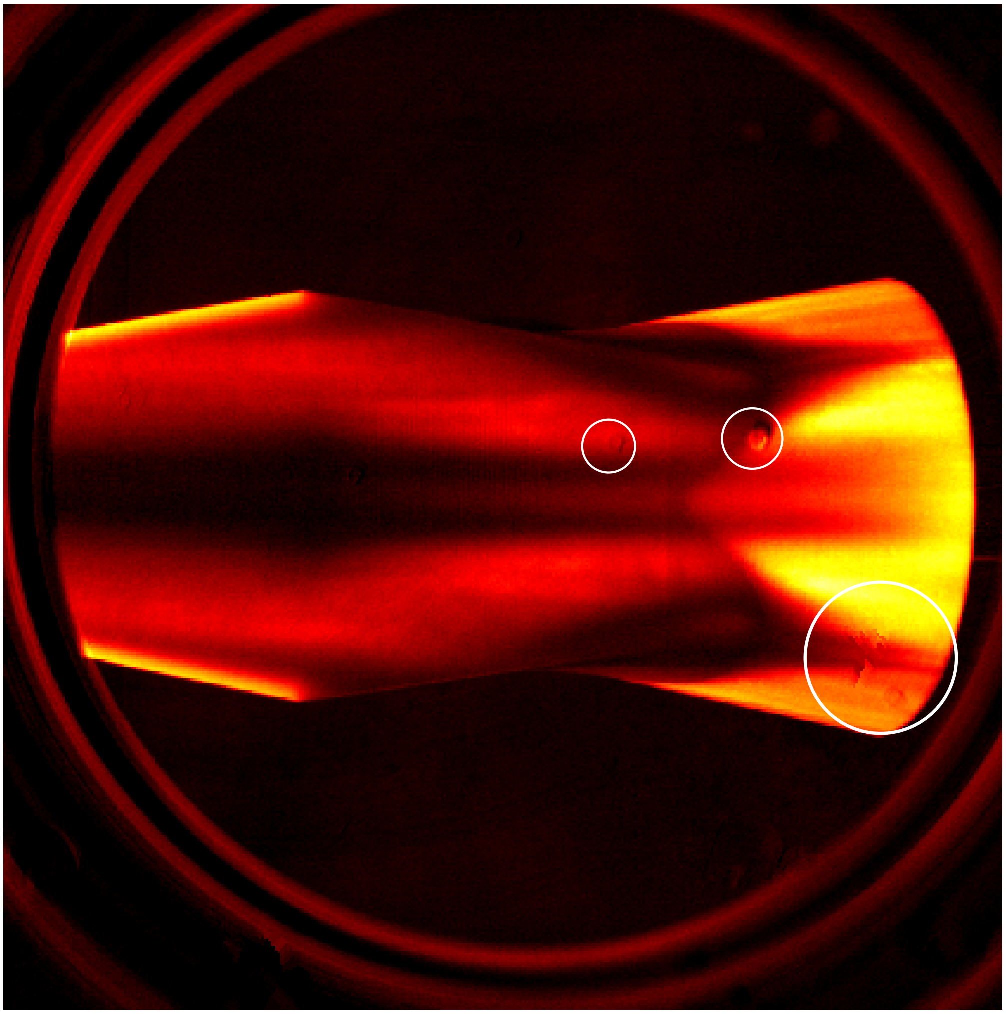

Figure 3.25: ACE wind tunnel glass imperfections

In all comparisons made major heat flux features identified in steady state CFD solutions were also observed in heat flux calculated from wind tunnel test data. This correlation between ACE wind tunnel test results and CFD data provides qualitative evidence supporting the results found using CFD.

4. CONCLUSIONS AND RECOMMENDATIONS

The goal of this work was to model heat flux on the BOLT-II flight test vehicle in the vicinity of the fairing and payload bay using CFD simulations to support thermal protection calculations being performed at CUBRC and JHAPL. These simulations were performed using the US3D CFD code to analyze flowfields on structured grids generated in Pointwise.

4.1 Conclusions

CFD simulations were performed for the conditions listed in Table 2.1 and Table 2.2 based on critical points identified along the simulated BOLT-II trajectory and a previously identified condition of intense heat flux. These simulations revealed that a significant amount of heat flux occurs on the conical transition of the payload bay downstream from the low radius edge of the fairing and that very little heat flux occurs on the cylindrical section of the payload bay behind the conical transition. Further investigation of the flowfield revealed that as flow moves along the low radius edge of the fairing the boundary layer experiences significant deformation and that wingtip vorticity from the BOLT-II flight vehicle directly interacts with, and causes, the spots of intense heat flux on the payload bay. Angles of attack in both α and β increase heat flux at these spots by creating increased amounts leading edge vorticity. Heat flux observed on the fairing was highest behind the BOLT-II test surface and followed patterns that were a direct continuation of heat flux on BOLT-II. Angles of attack in α created the most significant increases in heat flux at this spot due to the component of flow made incident to the test surface and the fairing behind it. For each simulation the maximum heat flux observed on the payload bay and fairing were recorded.

To establish the dependence of CFD heat flux results on the turbulence model being used one simulation condition was run a second time using a diferent turbulence model. Comparisons of solutions found using the two different turbulence models showed good agreeance and the maximum heat flux values on both the fairing and payload bay were found to have less than a 0.1% difference between the two simulations.

Further comparisons of CFD heat flux results were made to wind tunnel tests which were conducted using a 25% scale model of the geometry of interest on the flight vehicle. Heat flux data was calculated for wind tunnel tests using IR imaging techniques and a 1D heat flux code. Comparing this to CFD at trajectory conditions it was observed that all major heat flux features seen in CFD could be identified in wind tunnel tests. To allow for direct comparison of CFD and wind tunnel test data a 25% scale mesh was run in CFD using wind tunnel test conditions in the free stream and the Stanton number at the wall was calculated for CFD and wind tunnel results to account for boundary condition differences at the wall. Comparison of the results showed that CFD slightly over-predicts heat flux at the wall but obtains results at a similar magnitude and correctly predicts all heat flux patterns observed in wind tunnel tests. Although features observed were found to be much less distinct, the heat flux data from wind tunnel tests exhibited the same major features as heat flux in all CFD simulations. The agreement of all major heat flux features between these two tests provides qualitative evidence supporting the results obtained from CFD simulations.

4.2 Recommendations

The current analysis performed limited the angles of attack to being purely in α or purely in β. To gain an understanding of the heat flux behavior at mixed angles of attack it is recommended that a more detailed set of angles is run including simulations with angles of attack in both α and β.

REFERENCES

[1] Pope, S., *Turbulent Flows*, Cambridge University Press, 2000.

[2] Wheaton, B. M., Berridge, D. C., Wolf, T. D., Stevens, R. T., and McGrath, B. E., “Boundary Layer Transition (BOLT) Flight Experiment Overview,” *2018 Fluid Dynamics Conference*, 2018, doi: 10.2514/6.2018-2892.

[3] Thome, J., Dwivedi, A., Nichols, J. W., and Candler, G. V., “Direct Numerical Simulation of BOLT Hypersonic Flight Vehicle,” *2018 Fluid Dynamics Conference*, 2018, doi: 10.2514/6.2018-2894.

[4] Anderson, J., *Hypersonics and High-Temperature Gas Dynamics*, AIAA, 2019.

[5] Liepmann, H. and Roshko, A., *Elements of Gasdynamics*, Dover Publications, 1985.

[6] White, F., *Viscous Fluid Flow*, McGraw Hill, 2006.

[7] Anderson, J., “Ludwig Prandtl’s Boundary Layer,” *Physics Today*, Vol. 58, No. 12, 2005, pp. 42–48, doi: 10.1063/1.2169443.

[8] Prandtl, L., “Motion of Fluid With Very Little Viscosity,” Tech. Rep. 452, NACA, 1927.

[9] Blasius, H., “Grenzschichten in Flüssigkeiten mit Kleiner Reibung,” *Zeitschrift für angewandte Mathematik und Physik*, Vol. 56, 1908, pp. 1–37.

[10] Von Karman, T. and Tsien, H., “Boundary Layer in Compressible Fluids,” *Journal of the Aeronautical Sciences*, Vol. 5, No. 6, 1938, pp. 227–232, doi: 10.2514/8.591.

[11] VanDriest, E., “The Problem of Aerodynamic Heating,” *Aeronautical Engineering Review*, 1956, pp. 26–41.

[12] DeJarnette, F., Hamilton, H., Weilmuenster, J., and Cheatwood, M., “A Review of Some Approximate Methods Used in Aerodynamic Heating Analyses,” *Journal of Thermophysics*, Vol. 1, No. 1, 1987, pp. 5–12, doi: 10.2514/3.1.

[13] Anderson, J., *Fundamentals of Aerodynamics*, McGraw Hill, 2017.

[14] Shang, J. and Scherr, S., "Navier-Stokes Solution for a Complete Re-Entry Configuration," *Journal of Aircraft*, Vol. 23, No. 12, 1986, pp. 881–888, doi: 10.2514/3.45396.

[15] Pletcher, R., Tannehill, J., and Anderson, D., *Computational Fluid Mechanics and Heat Transfer*, CRC Press, 2013.

[16] Johnson, F., Tinoco, E., and Yu, N., "Thirty Years of Development and Application of CFD at Boeing Commercial Airplanes, Seattle," *Computers and Fluids*, Vol. 34, 2005, pp. 1115–1151, doi: 10.1016/j.compfluid.2004.06.005.

[17] Candler, G., Johnson, H., Nompelis, I., Subbareddy, P., Drayna, T., Gidzak, V., and Barnhardt, M., "Development of the US3D Code for Advanced Compressible and Reacting Flow Simulations," *53rd AIAA Aerospace Sciences Meeting*, 2015, doi: 10.2514/6.2015-1893.

[18] Semper, M., Pruski, B., and Bowersox, R., "Freestream Turbulence Measurements in a Continuously Variable Hypersonic Wind Tunnel," *50th AIAA Aerospace Sciences Meeting including the New Horizons Forum and Aerospace Exposition*, 2012, doi: 10.2514/6.2012-732.

[19] Leidy, A., *An Experimental Characterization of 3D Transitional Shock Wave Boundary Layer Interactions at Mach 6*, Ph.D. thesis, Texas A&M University, 2019.

[20] Neel, I. T., Leidy, A., Tichenor, N. R., and Bowersox, R., "Characterization of Environmental Disturbances on Hypersonic Crossflow Instability on the HIFiRE-5 Elliptic Cone," *22nd AIAA International Space Planes and Hypersonics Systems and Technologies Conference*, 2018, doi: 10.2514/6.2018-5375.

[21] Kostak, H., Bowersox, R. D., McKiernan, G., Thome, J., Candler, G. V., and King, R., "Freestream Disturbance Effects on Boundary Layer Instability and Transition on the AFOSR BOLT Geometry," *AIAA Scitech 2019 Forum*, 2019, doi: 10.2514/6.2019-0088.

[22] Johnston, Z. M. and Candler, G. V., "Hypersonic Simulations of the BoLT-II Subscale Geometry," *AIAA Scitech 2021 Forum*, 2021, doi: 10.2514/6.2021-0366.